



Rapporti Tecnici INAF INAF Technical Reports

Number	187
Publication Year	2022
Acceptance in OA@INAF	2022-10-17T13:59:21Z
Title	Fisheye Lens Geometric Calibration
Authors	CORAN, GIACOMO; SIMIONI, EMANUELE; PERNECHELE, Claudio; LESSIO, Luigi
Affiliation of first author	O.A. Padova
Handle	http://hdl.handle.net/20.500.12386/32696 ; https://doi.org/10.20371/INAF/TechRep/187

TR02 – FISHEYE LENS GEOMETRIC CALIBRATION

14/10/2022

G. Coran ⁽¹⁾, E. Simioni⁽¹⁾, C. Pernechele⁽¹⁾, L. Lessio⁽¹⁾

(1) INAF OSSERVATORIO ASTRONOMICO DI PADOVA
Vicolo Osservatorio 5 - 35122 - PADOVA.

Index of contents

1	INTRODUCTION	3
1.1	Approval	3
1.2	Acknowledgments	3
1.3	Reference Documents	3
1.4	Acronyms	4
2	SCOPE OF THE TR	5
3	CALIBRATION METHOD	6
3.1	Geometrical projective model	6
3.1.1	Single effective viewpoint constrains	6
3.1.2	Camera model	7
3.2	OCAMCALIB estimation method	9
3.2.1	Automatic or Manual Extra	9
3.2.2	Calibration	9
3.2.3	Reprojection on Images and Extrinsic Validation	10
3.2.4	Intrinsic Parameters Visualization	12
3.3	Common mapping function	12
4	APPLICATION ON THE FISH-EYE LENS	13
4.1	Lens description	13
4.2	Set of images and calibration target	13
5	RESULTS	16
5.1.1	Residual analysis	17
5.1.2	IFOV measurement	21
5.1.3	Lens constant	22
6	Table of data results	27

1 INTRODUCTION

1.1 Approval

Edited by	G. Coran
Revised by	E. Simioni
Approved by	C. Pernechele

1.2 Acknowledgments

This work has been funded by ASI (contract n. 2020-4-HH.0) for the Italian participation to the phase-0 study of ESA Comet Interceptor EnVisS camera.

1.3 Reference Documents

- [1] G. Coran, E. Simioni, C. Pernechele e L. Lessio, «Hyperhemispheric Lens Geometric Calibration,» INAF, Padova, 2022.
doi: 10.20371/INAF/TechRep/174
- [2] D. Scaramuzza, A. Martinelli e R. Siegwart, «A Toolbox for Easily Calibrating Omnidirectional Cameras,» in *IEEE/RSJ International Conference on Intelligent Robots and Systems*, 2006.
- [3] G. Cremonese, F. Capaccioni, M. Capria e al., «SIMBIO-SYS: Scientific Cameras and Spectrometer for the BepiColombo Mission,» *Space Science Reviews*, vol. 216, n. 5, pp. 1-78, 2020.
- [4] E. Simioni e al., «SIMBIO-SYS/STC stereo camera calibration: Geometrical distortion,» *Review of Scientific Instruments*, vol. 90, n. 4, 2019.
- [5] D. Scaramuzza, «OCamCalib,» [Online]. Available: <https://sites.google.com/site/scarabotix/ocamcalib-omnidirectional-camera-calibration-toolbox-for-matlab>.
- [6] M. Rufli e al., «Automatic Detection of Checkerboards on Blurred and Distorted Images,» in *2008 IEEE/RSJ International Conference on Intelligent Robots and Systems, IROS*, Nice, France, 2008.
- [7] C. Pernechele, *Introduction to Panoramic Lenses*, vol. SL38, S. o. P. I. Engineers, A cura di, Bellingham, Washington: SPIE Press, 2018.

1.4 Acronyms

FEL	Fish-Eye Lens
FOV	Field Of View
IFOV	Instantaneous Field Of View
LM	Levenberg-Marquadt
OCAMCALIB	Omnidirectional Toolbox
SSRE	Sum of Squared Reprojection Errors
SVD	Singular Value Decomposition
TR	Technical Report

2 SCOPE OF THE TR

In this report we will show the calibration procedure and the obtained results for the definition of the intrinsic parameters of a wide-angle system through the use of a set of acquisitions of a well-known calibration target. In this case the method is applied to a Fujinon fish-eye camera hereafter called FEL (Fish-Eye Lens).

3 CALIBRATION METHOD

Fish-eye lenses are usually not central systems and even if they approximate the single viewpoint property, we decided to analyze the FEL with the same general approach explained and used in a previous work [1]. It is possible to model the camera projection as two subsequent steps:

- an orthogonal projection
- a following reflection through a symmetric mirror defined by polynomial coefficients.

This approach is developed in MATLAB Omnidirectional Toolbox (OCAMCALIB) [2].

The approach is based on the acquisitions of images of a well-known target positioned in the different acquisitions in manner to acquire its images uniformly distributed in the FOV (Field Of View) of the camera.

Thanks to this approach we were able, without the use of rotational or mechanical components (i.e. hexapod [3] or series of rotational system to manage mirrors and light source [4] to obtain the intrinsic parameters (the model of the payload) and the target extrinsic parameters (the position and the orientation of the target in the world space), and, with a further improvement, even data on the relation between various parameters and the calibration errors. From those data with a later iterative analysis we were able to measure the values for the constants defining the mapping function of the FEL.

The camera model will be explained in the next section 3.1, in section 3.2 we will show the intrinsic and target calibrations and in section 3.3 we will briefly discuss the requirements of the mapping function.

3.1 Geometrical projective model

3.1.1 Single effective viewpoint constrains

The model used in the following analysis was developed for a camera which did not have central characteristics, although the approach is general enough to be applied even in the case of the FEL. Central and non-central designs are shown in Figure 3.1. Even if, as said earlier, the FEL approximates the single viewpoint property, we looked for the relation existing in non-central configurations between a given 2D pixel point of the image plane and the 3D direction coming from the equivalent mirror surface effective viewpoint. This can be performed by OCAMCALIB [5] under limited assumptions.

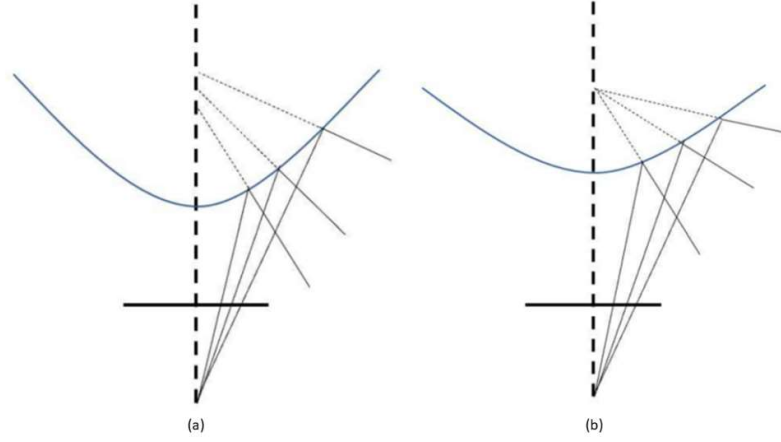


FIGURE 3.1 IN (A) A CAMERA-MIRROR ASSEMBLY NON-CENTRAL (I.E. NON-SINGLE EFFECTIVE VIEWPOINT) SYSTEM WHERE THE OPTICAL RAYS COMING FROM THE CAMERA AND REFLECTED BY THE MIRROR SURFACE DO NOT INTERSECT INTO A UNIQUE POINT; IN (B) A CENTRAL CAMERA WHERE THE SINGLE EFFECTIVE VIEWPOINT PROPERTY IS PERFECTLY VERIFIED; IN BOTH CASES A NON-ORTHOGRAPHIC PROJECTION IS USED TO MODEL THE IMAGE PLANE FORMATION

3.1.2 Camera model

The model proposed associates the homogenous coordinates $u' \in \mathbb{R}^3$ in the sensor reference system (centered in C' in Figure 3.2) to a coaxial reference system (C'' , called here after “center of the camera”) following an affine transformation:

$$u'' = Au' \quad (3.1)$$

where $A \in \mathbb{R}^{3 \times 3}$ is an affine transformation which well approximates possible off-axis misalignment between the orthonormal projection and the equivalent mirror symmetrical axis.

The relation between a 3D point $X \in \mathbb{R}^4$ (expressed in homogeneous coordinates) and the coaxial reference system coordinates can be expressed by:

$$v = g(u'') \quad (3.2)$$

where the versor v represents the optical ray associated to the pixel and g is rotationally symmetric non-linear function representing the mirror. In the case of non-central cameras (see Figure 3.2b) this definition is not associated to a central point. In the case of central cameras (see Figure 3.2c) the versor satisfied even the equation:

$$\lambda v = PX, \lambda > 0 \quad (3.3)$$

where, $P \in \mathbb{R}^{3 \times 4}$ is the projection matrix centered for catadioptric systems in the focus of the parabolic or hyperbolic shape mirror.

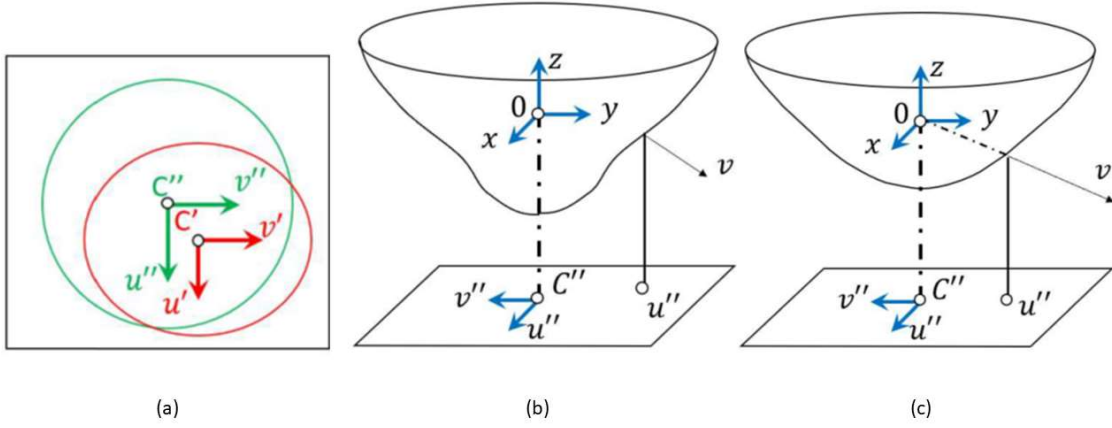


FIGURE 3.2 IN (A) THE SENSOR PLANE IN METRIC COORDINATES (IN GREEN) AND THE OVERLAPPED CAMERA IMAGE PLANE (IN RED). THE TWO SYSTEMS ARE RELATED BY AN AFFINE TRANSFORMATION. IN (B) GENERIC NON-CENTRAL CAMERA MODEL BASED ON RADIAL SYMMETRICAL MIRROR. IN (C) CENTRAL MODEL CONVERGENT ON THE ORIGIN REFERENCE SYSTEM

In the case of the omnidirectional camera it is assumed that the function g is rotationally symmetric with respect to the sensor normal axis on the boresight. Following this Eq. (3.2) assumption can be rewritten as:

$$\theta = \phi(\rho) \quad (3.4)$$

where ρ is the distance in pixels of the projected point from the camera center in the u'', v'' reference system and θ is the zenith angle of the chief ray respect to the horizon plane, positive in the hemisphere full covered.

We propose two different solutions and the definition of the ϕ function. Both the solutions use an N order polynomial here after indicated as:

$$p(\rho) = \sum_{i=0}^N p_i \rho^i \quad (3.5)$$

or as FPF (Forward Projective Function).

First solution is a simple “direct model” where the chief ray is defined by the same polynomial function:

$$\theta = p(\rho) \quad (3.6)$$

A more “physical approach” defines the chief ray as:

$$\tan(\theta) = -\frac{\rho}{p(\rho)} \quad (3.7)$$

The direct model returns a more constrained camera model. The simplicity of the model allows for instance to add as vinculum the monotony of the IFoV (simple derivative of the p function). On the other side, physical approach reaches the best performance but making not possible to impose any additive vinculum. This brings to a not correct interpretation of the geometry of the camera model in the outer regions of the field of view. The two models’ main equations, including the solver used in the nonlinear regression methods of the different stages of the calibration are reported in TABLE 1.

Direct Model	
Chief Ray	$\theta = p(\rho)$
IFoV	$\dot{\theta} = \dot{p}(\rho)$
Solver	$p_0 - \theta + p_1\rho + \dots + p_N\rho^N = 0$
Physical Model	
Chief Ray	$\tan(\theta) = \frac{\rho}{p(\rho)}$
IFoV	$\dot{\theta} = -\frac{p + \dot{p}\rho}{p^2 + \rho^2}$
Solver	$p_0 + (p_1 - \tan(\theta))\rho + \dots + p_N\rho^N = 0$

TABLE 1 MAIN EQUATIONS OF THE SIMPLE AND PHYSICAL MODELS DEVELOPED

TABLE 1 reports even the IFoV as derivative of the zenith angle with respect to the pixel distance from the center. Note that while in the first case it assumes a polynomial form for the chief ray, in the physical model it is defined by a rational model which reaches at denominator two time the magnitude of the polynomial order.

3.2 OCAMCALIB estimation method

We used an estimation method developed by Scaramuzza on MATLAB.

The method utilizes a code able to recognize a chessboard inside an image acquired with a generic lens (in this approach a hyperhemispheric one) and detect the corner points thanks to a Harry extractor.

3.2.1 Automatic or Manual Extra

First, we must load the images and extract the corner points, which are the crossing point within four squares. It is required to define the number of squares along the two axes of the chessboard and the dimension of the side of a square, which in our case is 42.5 mm.

The code can automatically identify the corners, asking for user supervision only if it is not able to recognize all the corners that should be present. Corners are detected following a specific approach based on Harris detection. The algorithm works by analyzing the eigenvalues of the 2D discrete structure tensor matrix at each image pixel and flagging a pixel as a corner when the eigenvalues of its structure tensor are sufficiently large. The algorithm has a satisfying detection rate of 95% and an accuracy less than 0.5 px [6].

In any case, the user is always able to identify manually all the corners in case of images with focus or saturation problems.

The code requires an initial central point for the lens, with a default option being the central point of the image, so half the height and half the width. This is only an initial value since the code will then constrain the true position of the center in a later step, as explained in Section 3.2.2.1.

3.2.2 Calibration

The code calibrates the optical system starting from the images and knowing the target dimension (in the chessboard case the chess one).

It estimates at the same time the intrinsic parameters and the angular target parameters (position and orientation of the chessboards in the real world) by minimizing the residuals of the projected points via Singular Value

Decomposition (SVD) taking advantage of the orthogonality of the grid. In this way the code defines completely the rototranslation from the reference system of the target to the camera reference system.

As intrinsic parameters it considers the affine transformation and the radial function, described in Eq. (3.6), parametrized with a polynomial model which DOFs (degree of freedom) can be chosen by the user. Both the mapping function could be a study case in case, for refinement, we would test different projection as homography or different symmetrical functions as spline based. For the following analysis, a fourth-degree polynomial equation was used. The final missing parameters of the positions of the chessboards in the camera space are then defined estimating the polynomial parameters via a simple least-squares solution, which also better defines the polynomial solution and the affine transformation.

The code returns this first estimation of the coefficients.

3.2.2.1 Find Center

The model is strongly dependent on the center position of the image on the sensor (Figure 3.2a) which, when incorrectly defined, not only corresponds to misalignment of the symmetric axis but also has the effect of increasing the weight of the reprojection error.

Via iterative image analysis the code is able to identify the true coordinates of the average center of the lens on the sensor minimizing globally the Sum of Squared Reprojection Errors (SSRE), making up for the chance of a lens not centered with the sensor.

3.2.2.2 Calibration Refinement

Once the image center is obtained, we can recalibrate the polynomial equation with the newly acquired information. The affine transformation, the polynomial definition of the mirror and the position and attitude of the targets are defined by non-linear optimization of the residuals thanks to Levenberg-Marquadt (LM) approach. From the estimated solution the algorithm refines the target and intrinsic parameters separately in a two steps iterative process, firstly refining the target parameters ignoring the intrinsic ones and then using the just estimated target parameters to refine the intrinsic ones. The results obtained with this step usually greatly improve the estimation obtained with the first calibration.

3.2.3 Reprojection on Images and Extrinsic Validation

The code is able to re-project the corners re-calculated with the new polynomial calibration on the images, reconstructing the chessboards as in Figure 3.3 and showing the deviation from the initially detected corners, visible in Figure 3.4.

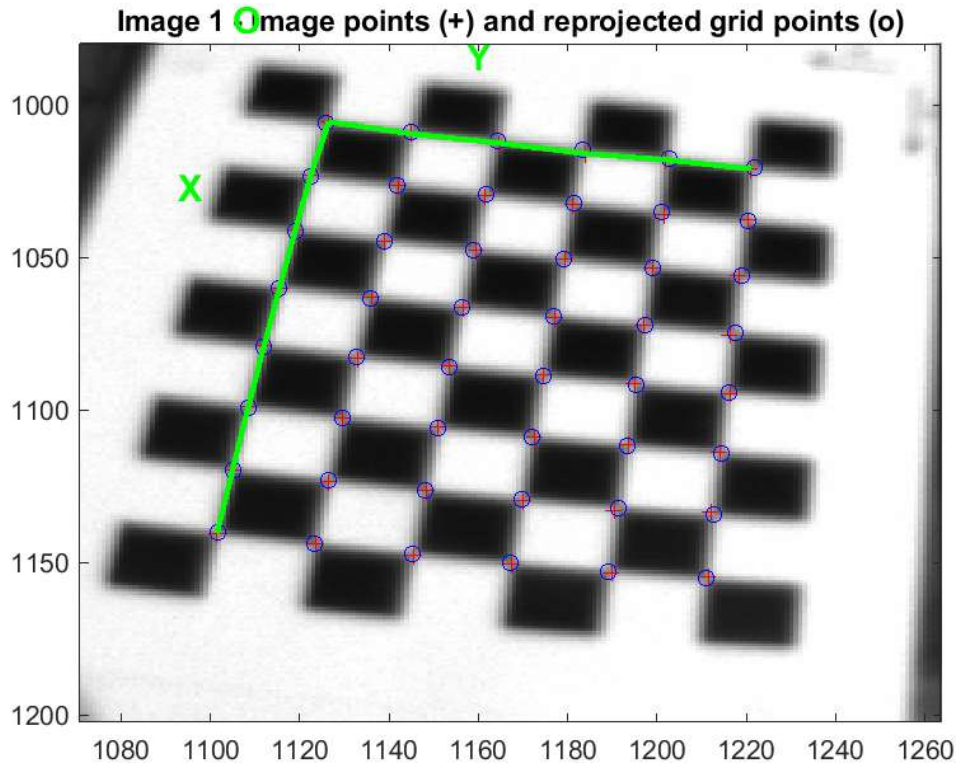


FIGURE 3.3 EXAMPLE OF RECONSTRUCTED CHESSBOARD WITH THE INITIALLY DETECTED CORNERS IN RED AND RECOMPUTED CORNERS IN BLUE

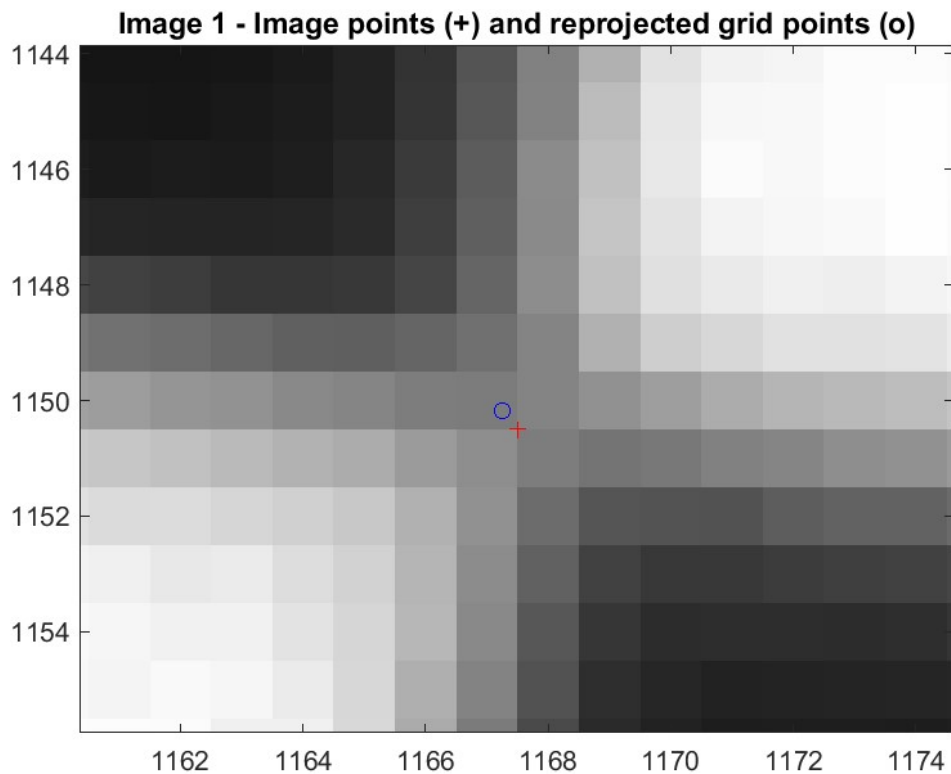


FIGURE 3.4 EXAMPLE OF DEVIATION BETWEEN THE INITIAL AND THE RECOMPUTED CORNERS

3.2.4 Intrinsic Parameters Visualization

The code can display the 3-D positions of the chessboards with respect to lens, as well as the recalibration errors, the forward projection function, and the angle of the optical ray with respect to distance from the image center in pixels.

The original code was modified in order to display additional plots.

The relation between the zenith angle and the recalibration errors is important, showing if the method is working to determine the position of the corners with precision even at high zenith angles where the anamorphism of the lens is higher. The plot showing the relation between the azimuthal angle and the recalibration errors can display the eventuality of a lens out of focus towards a specific direction. The IFoV was calculated from the polynomial equation and can be displayed with our addendum. It is also possible to print all the detected corners from all the images on a single image with a color gradient showing the magnitude of the recalibration errors.

3.3 Common mapping function

As described in *"Introduction to Panoramic Lenses"* [7], the "perfect" undistorted map of the object space is given by:

$$\rho(Z) = d \tan(Z) \quad (3.8)$$

Every point in the space is mapped so that they maintain the same angular distribution into the focal plane and object straight lines remain straight (distortion free) in the image. This function is known as "perspective projection" and it is not meaningful for wide zenith angles because the focal plane would be infinitely wide, and the entrance pupil would be completely obscured at $Z = 90^\circ$.

Then, to make a wide-angle lens useful for some applications, some degree of image distortion must be accepted, and this is done by adjusting the mirror curvature and asphericity.

The most general lens mapping function has the following form:

$$\rho(Z) = dk_1 \sin(k_2 Z) \quad (3.9)$$

where k_1 and k_2 are dimensional coefficients. Within this class of mapping functions, high compression of the marginal objects is present. We cite two types of projection which belong to this type of mapping functions:

• equisolid angle projection	$(k_1=2, k_2=0.5)$, i.e. $R=2 f(0) \sin(\theta/2)$ Which maintains surface relations. Each pixel in the detector subtends an equal solid angle, i. e. an equal area on the unit sphere.
• orthographic projection	$(k_1=k_2=1)$ where $R=f(0) \sin(\theta)$ This mapping function maintains planar illuminance. In this projection the marginal fields are extremely compressed at the focal plane and make sense only for $\theta < 90^\circ$.

4 APPLICATION ON THE FISH-EYE LENS

4.1 Lens description

We tested the calibration method using the Fujinon FE185C046HA-1 fish-eye lens displayed in Figure 4.1.



FIGURE 4.1 THE FUJINON FE185C046HA-1 FISH-EYE LENS USED IN OUR TEST

The lens has a C mount, a 1.4mm focal length, a variable aperture from F1.4 to F16, which was used at the minimum for this test, is designed for high resolution, up to 5 megapixel, and has a wide angle FoV of 185°. All perfectly fits the Basler Ace acA2440-35um image sensor, which has a 2/3-in. format and allows for 2448x2048 pixels large images with a pitch size of 3.45 μm .

4.2 Set of images and calibration target

The lens was mounted on an arm support with a line of sight parallel to the ground.

For the lens analysis we used a set of images displayed in Figure 4.2, with a clearer example in Figure 4.3. The set consists of 19 images at mid to large distances, covering a wide zenithal angle range.

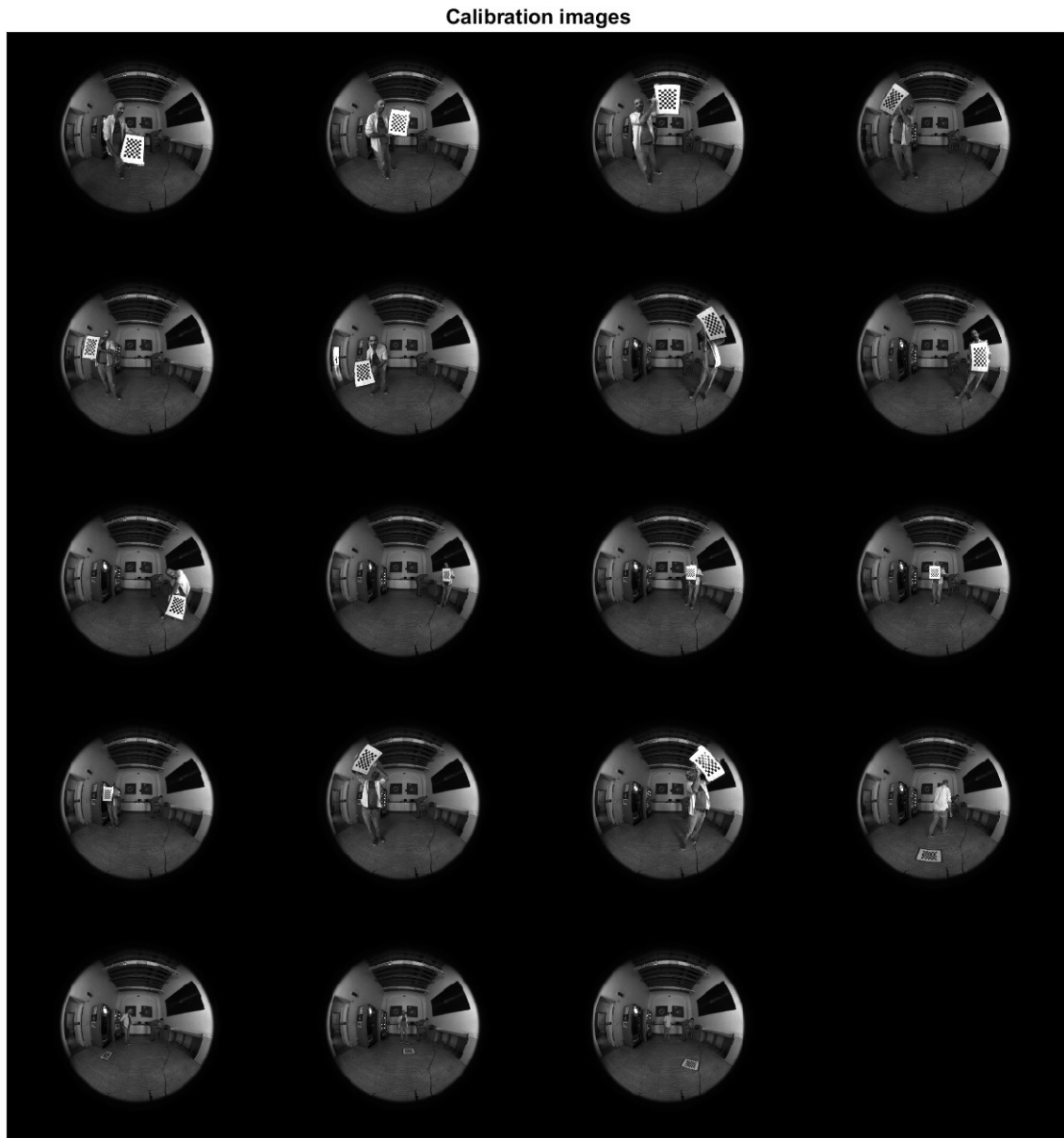


FIGURE 4.2 *IMAGE SAMPLE*



FIGURE 4.3 *EXAMPLE OF AN IMAGE OF THE SAMPLE*

The chessboard, printed and fix on a rigid glass support, is composed by a 7 by 5 grid of black and white squares, with a 42.5 cm side. The images show the chessboard from several positions and orientations, covering almost 360° in azimuthal angle.

The code was not able to automatically recognize all the corners in 9 images from the set. Out of the 9 images, 7 required the complete manual detection of the corners, while for the other 2 only the completion of the detection was necessary.

5 RESULTS

In the following subsections the analysis results will be uncovered and discussed.

The calibration defined for each image the position and the attitude of the target. A plot of the result of this estimation is shown in Figure 5.1.

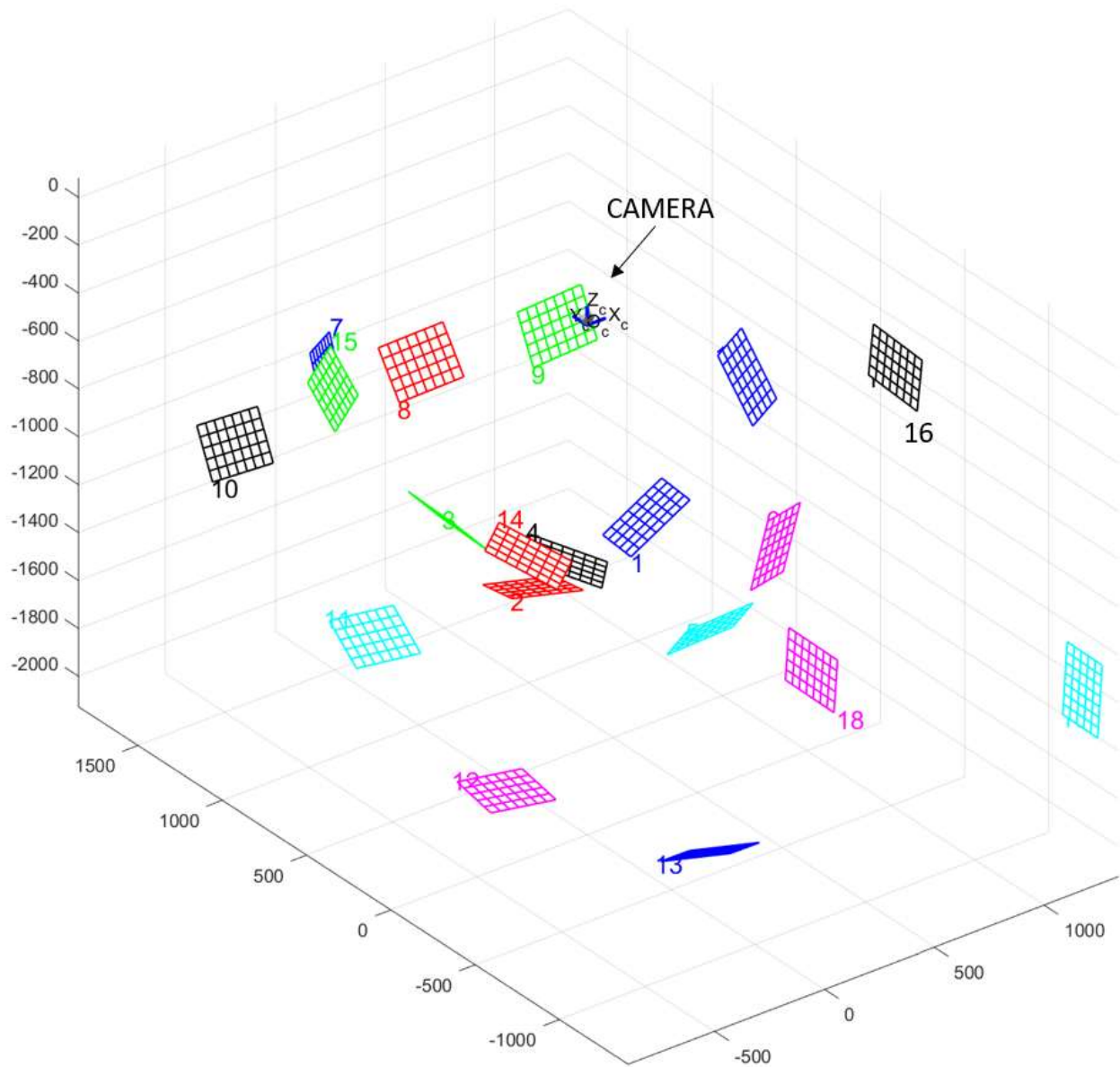


FIGURE 5.1 A PICTURE OF THE SIMULATOR SHOWING THE CALIBRATION PATTERNS AND THE VIRTUAL OMNIDIRECTIONAL CAMERA AT THE AXIS ORIGIN AFTER THE CALIBRATION, ALL THE PARAMETER CAN BE ACCESSED IN THE TOOL THROUGH THE STRUCTURE "OCAM_MODEL". AXES UNIT IS IN MM.

5.1.1 Residual analysis

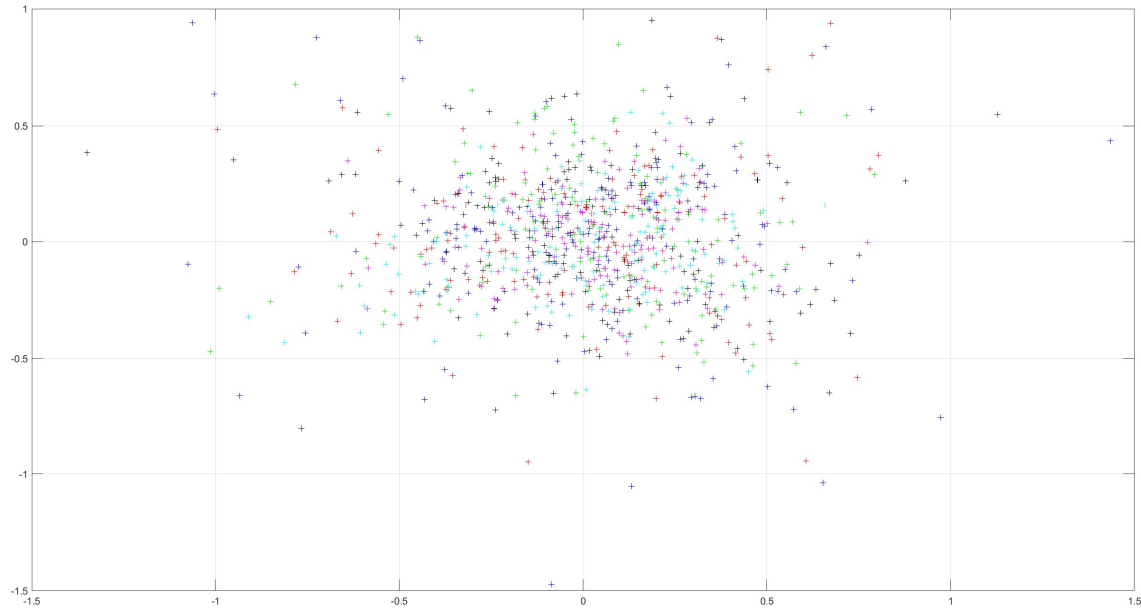


FIGURE 5.2 *RESIDUALS DISTRIBUTION*

Residuals, displayed in Figure 5.2, show a very constrained variation in the position of the corners obtained with the calibration.

Horizontal and vertical errors in reprojection are limited to standard deviation values of 0.3224 and 0.2936 px respectively, meaning that most of the residuals of the corners (including the camera model assumed in Section 3.1.2 and the detection) are within 0.8 px. The result can be compared with the measurement obtained by the algorithm in [1] where we underlined that the detection of the corners performed by Harry's corners reaches 0.5 px.

Figure 5.3 and Figure 5.6 show the dependence of the errors with the zenith and the azimuthal angles. As we can see there are no noticeable dependences on the zenith angle as on the azimuthal one. This suggests that the camera model assumed well represent the payload and that the quality of the images is not affected by possible defocusing or straylight effects which could impact the detection of the corners.

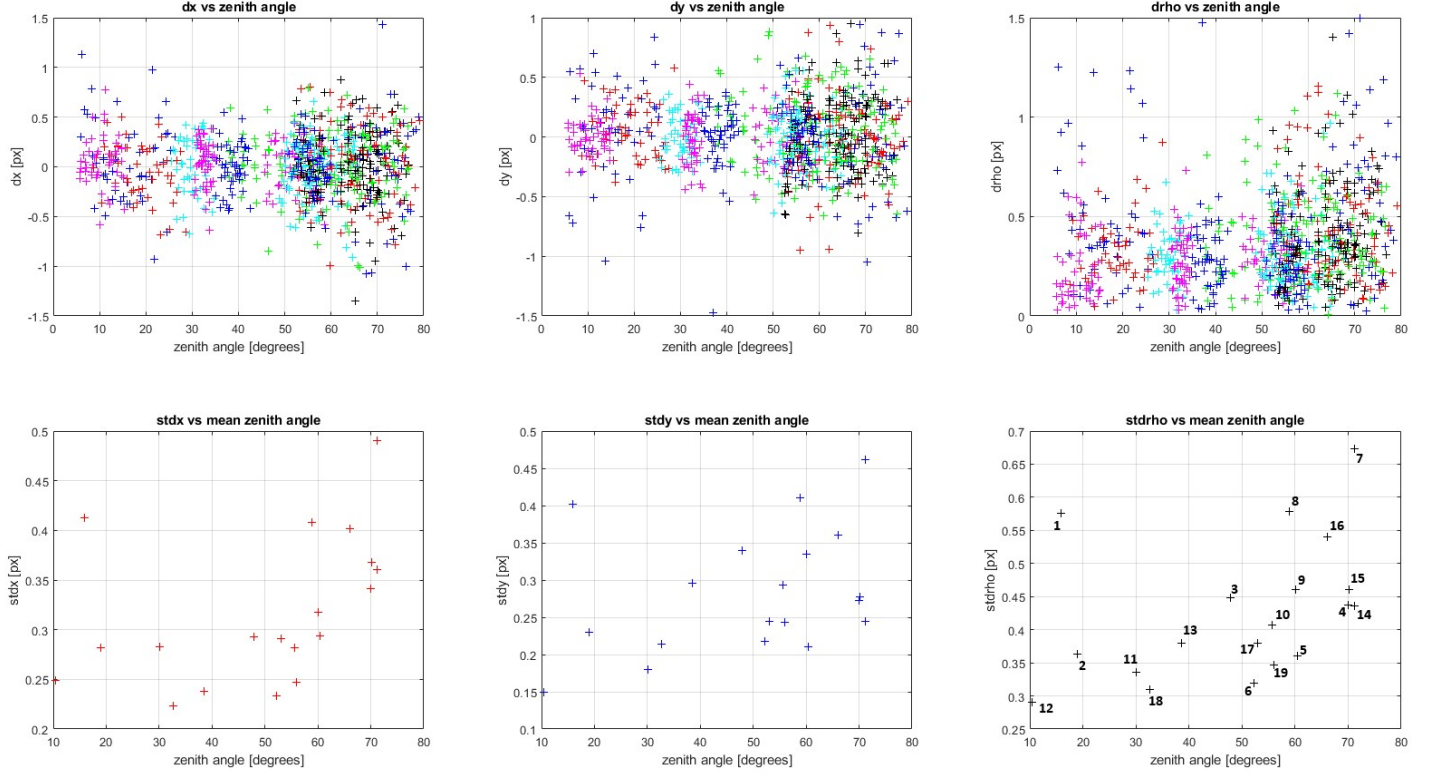


FIGURE 5.3 ON TOP: DISTRIBUTION OF THE CALIBRATION ERRORS (WITH DIFFERENT COLOR FOR EACH CHESSBOARD) WITH RESPECT TO THE ZENITH ANGLE. FIRST TWO PLOTS SHOW RESPECTIVELY THE HORIZONTAL AND VERTICAL ERROR OF THE REPROJECTION. ON BOTTOM: SAME PLOTS CONSIDERING THE MEAN ERROR OF EACH CHESSBOARD.

The plot shows a uniform distribution of the error with respect to the zenith angle. We find the three largest errors around 65° - 70° in zenith angle. Two of those errors belong to image 7, displayed in Figure 5.4, where residual are nominal for most of the corners but the central points in the second row from the bottom suffered of an imperfect detection and have errors equal to 1.4993 px and 1.4195 px respectively, the highest in the set. In image 16 (Figure 5.5) we can see the exception of the third corner having large error in the third row from the top and second column from the right, with an error equal to 1.4036 px. Since the average error is equal to 0.3682 px, these are almost 5 times larger. The high values for those specific errors are easily due to the large zenith angle and the distance from the camera system of the chessboards. However all the errors are definitely lower than what obtained in [1], so despite the three large errors most of the others are generally good, being under 1 px, which is enough to assure the validity of the model.

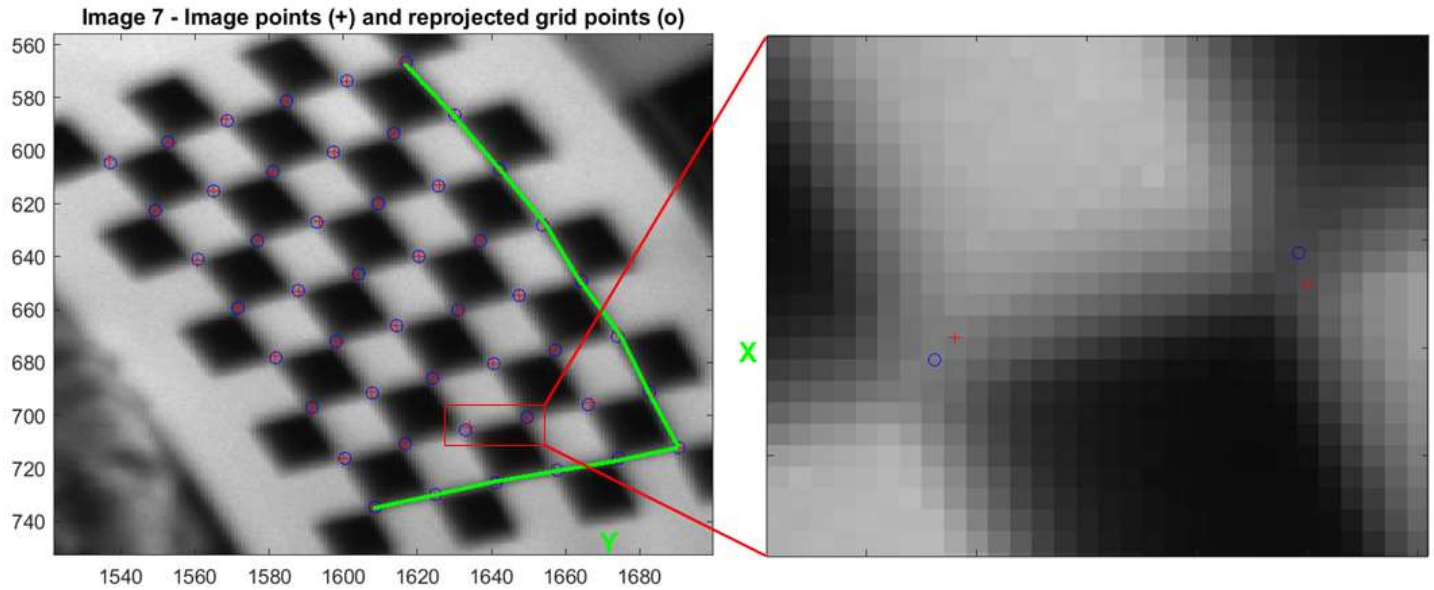


FIGURE 5.4 CASE OF IMAGE 7 WHERE REPROJECTION ERRORS ARE WORSE THAN EXPECTED. LEFT: THE WHOLE CHESSBOARD WITH ALL THE DETECTED AND REPROJECTED POINTS. RIGHT: THE TWO POINTS HAVING HIGH REPROJECTION ERRORS.

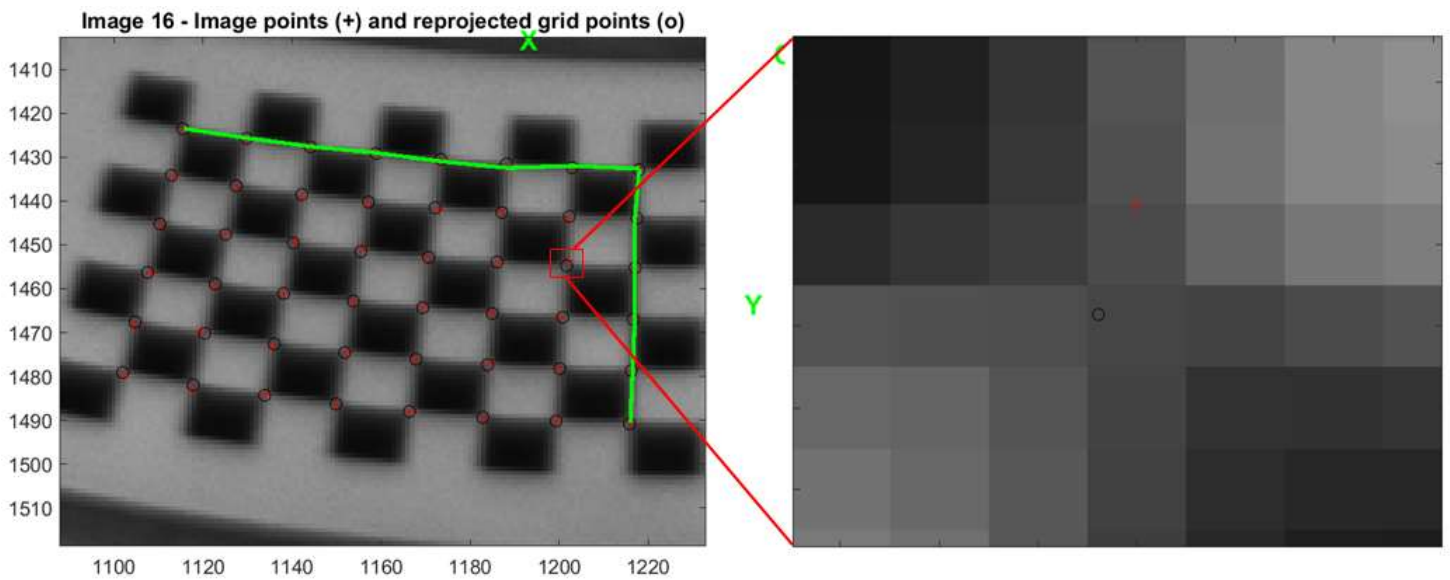


FIGURE 5.5 CASE OF IMAGE 16 WHERE REPROJECTION ERRORS ARE WORSE THAN EXPECTED. LEFT: THE WHOLE CHESSBOARD WITH ALL THE DETECTED AND REPROJECTED POINTS. RIGHT: THE POINT HAVING HIGH REPROJECTION ERRORS.

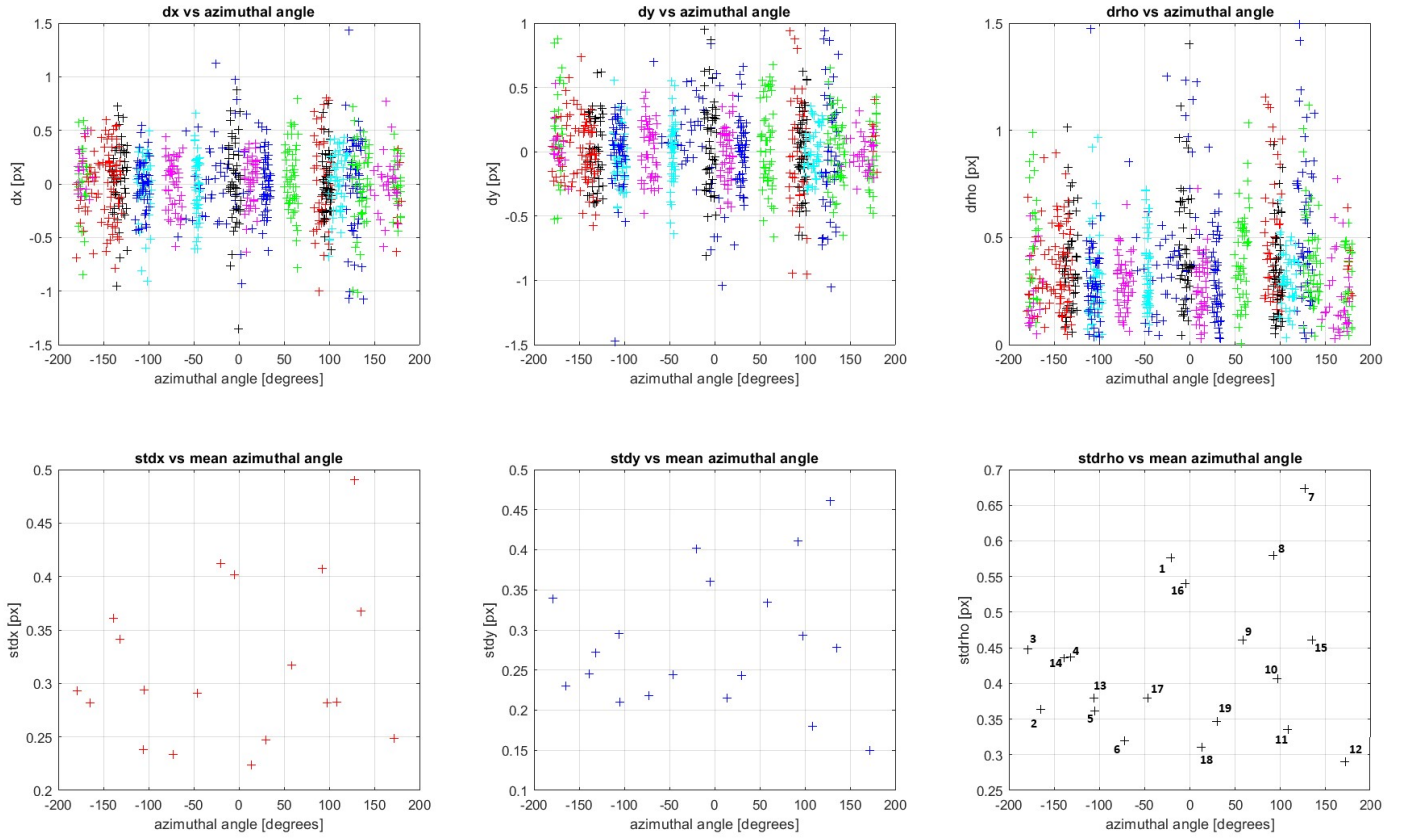


FIGURE 5.6 ON TOP: DISTRIBUTION OF THE CALIBRATION ERRORS (WITH DIFFERENT COLOR FOR EACH CHESSBOARD) WITH RESPECT TO THE AZIMUTHAL ANGLE. FIRST TWO PLOTS SHOW RESPECTIVELY THE HORIZONTAL AND VERTICAL ERROR OF THE REPROJECTION. ON BOTTOM: SAME PLOTS CONSIDERING THE MEAN ERROR OF EACH CHESSBOARD

Even in this case the plot shows no correlation between the residual errors and the azimuth, demonstrating that the affine transformation and the polynomial radial model are well representing the camera model. The highest errors are related to the same previously described corner points, but they are still confined within 1.5 px.

The code was even able to notice and correct a detection error due to an unfortunate user selection in one of the images where the corners were completely manually selected, shown in Figure 5.7. This case is not relevant in terms of the errors, since the point was initially manually selected, but it assures the validity of algorithm. The errors linked to this point is clearly visible both in the zenith and azimuthal plots, being the fourth highest errors.

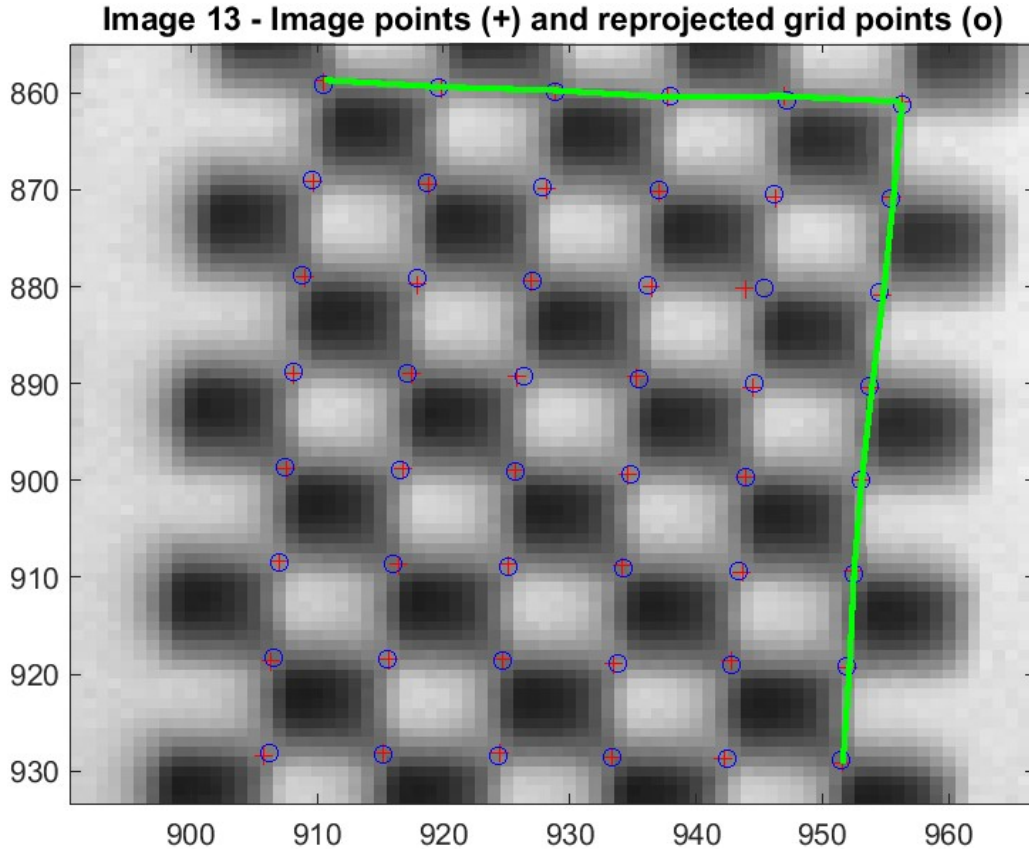


FIGURE 5.7 CASE OF IMAGE 13 WHERE REPROJECTION ERRORS IS DUE TO THE BAD MANUAL DETECTION; THE BAD CORNER IS ON THE THIRD ROW FROM THE TOP, SECOND COLUMN FROM THE RIGHT

5.1.2 IFOV measurement

Starting from the obtained polynomial model it was possible to estimate the IFOV of the system for each distance from the boresight. The IFOV is obtainable, as quoted in section 3.1.2, as the first derivative of Eq. (3.6):

$$\dot{\theta} = \dot{p}(\rho) \quad (5.1)$$

Results are displayed in Figure 5.8. The model application to the whole sensor shows the correct monotony of the IFOV, up to around 6 mrad/px at the edge. The images obtained with this lens are although confined within around 600 px from the image center, restricting the IFOV to around 1.2 at the worst in the outermost parts.

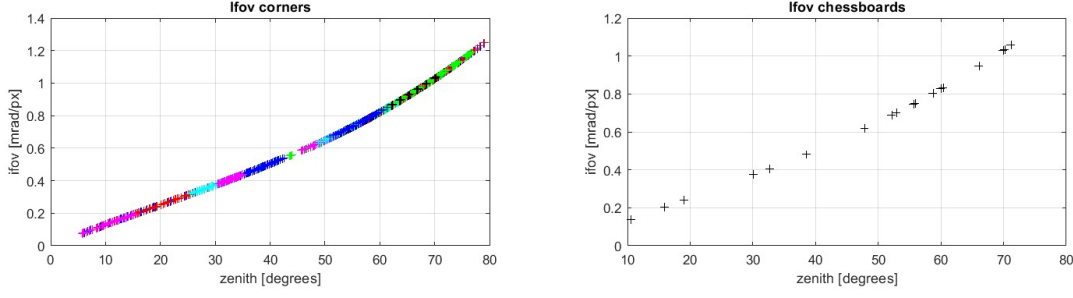


FIGURE 5.8 LEFT: IFOV OF THE SINGLE CORNERS; RIGHT: IFOV OF THE MEAN POINT OF EACH CHESSBOARD

5.1.3 Lens constant

As a final test we tried to obtain the constants k_2, dk_1 of the general lens mapping function, Eq. (3.9).

Firstly we searched for the values of the constants with a direct method. Since Eq. (3.9) is not analytically solvable an iterative research is necessary. From the starting equation, using two sets of values (Z_A, ρ_A) and (Z_B, ρ_B) , the following equation is derived:

$$\frac{\rho_A}{\rho_B} = \frac{dk_1 \sin(k_2 Z_A)}{dk_1 \sin(k_2 Z_B)} \quad (5.2)$$

where ρ and Z are the position of a corner on the sensor with respect to the lens reference system and its zenith angle, taken in pairs for two corners of the images (here identified by A and B).

The previous equation can be simplified as

$$\rho_A \sin(k_2 Z_B) - \rho_B \sin(k_2 Z_A) = 0. \quad (5.3)$$

We coupled each corner with all the other corners in the same image and looked by iteration for the correct value of k_2 . We moved k_2 inside the interval $]0.0001, 1.9999[$ by a 0.0001 step and kept the value which minimize the residual from the difference in Eq. (5.3). The extremes of the interval were chosen in this way since 0 and 2 are the minimum and the maximum values which set the argument of the sinus equal to 0 for the minimum and the maximum values among all the possible zenith angles for this lens, respectively. For each corner we took than the average value among all the couples. From each k_2 a value for dk_1 was then retrieved as

$$dk_1 = \frac{\rho}{\sin(k_2 Z)} \quad (5.4)$$

Results are shown in Figure 5.9 and Figure 5.10. The mean values for $k_2 = 0.1699 \pm 0.1074$ and $dk_1 = 10.9281 \pm 3.9285$. These values are then used as base values for a nonlinear least-squares algorithm, callable in MATLAB as “*lsqnonlin*”, which returns $k_2 = 0.1233$ and $dk_1 = 11.8537$. The residuals are calculated as the difference $\text{res} = \rho - dk_1 \sin(k_2 Z)$.

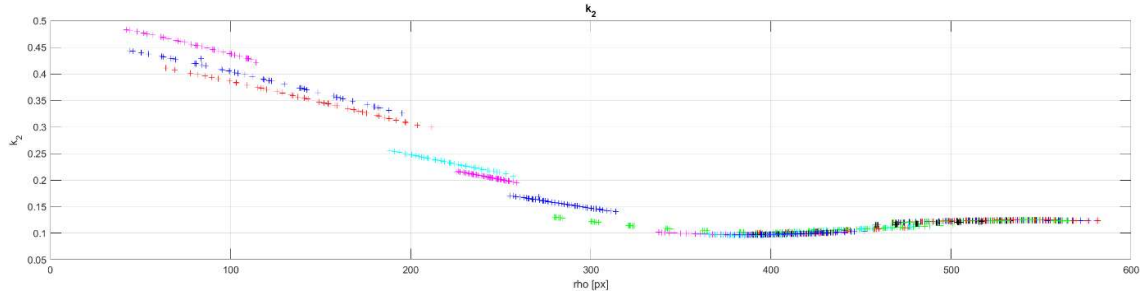


FIGURE 5.9 VALUES OBTAINED FOR THE CONSTANT k_2

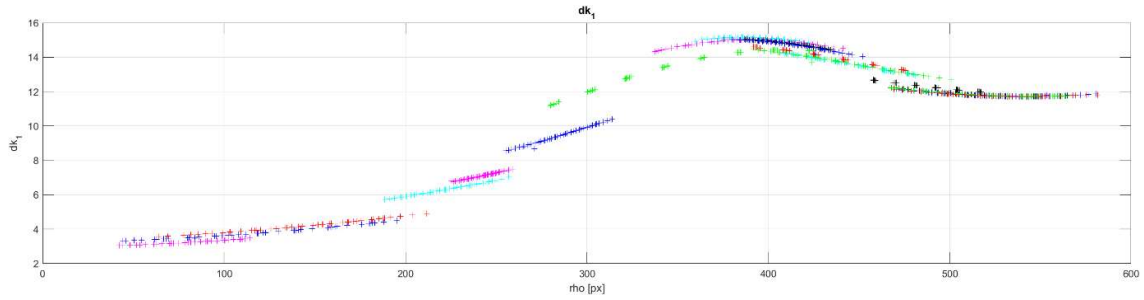


FIGURE 5.10 VALUES OBTAINED FOR THE CONSTANT dk_1

We repeated the analysis with a different approach. Using the values of the positions of the corners on the sensor with respect to the lens reference system ρ and their related zenith angle Z we applied the nonlinear least-squares evaluation separately on each single chessboard. The mean values for the constants obtained, averaged over all the chessboards, are $k_2 = 0.1231$ and $dk_1 = 12.1041$. This were subsequently used as base values for a nonlinear least-squares evaluation on all the corners of the chessboards, taken all together. The results of this independent evaluation are exactly the same as before, with $k_2 = 0.1233$ and $dk_1 = 11.8537$. In Figure 5.11 and Figure 5.12 are displayed the residuals of the methods in relation to the corners and to the distance ρ from the center of the lens projection.

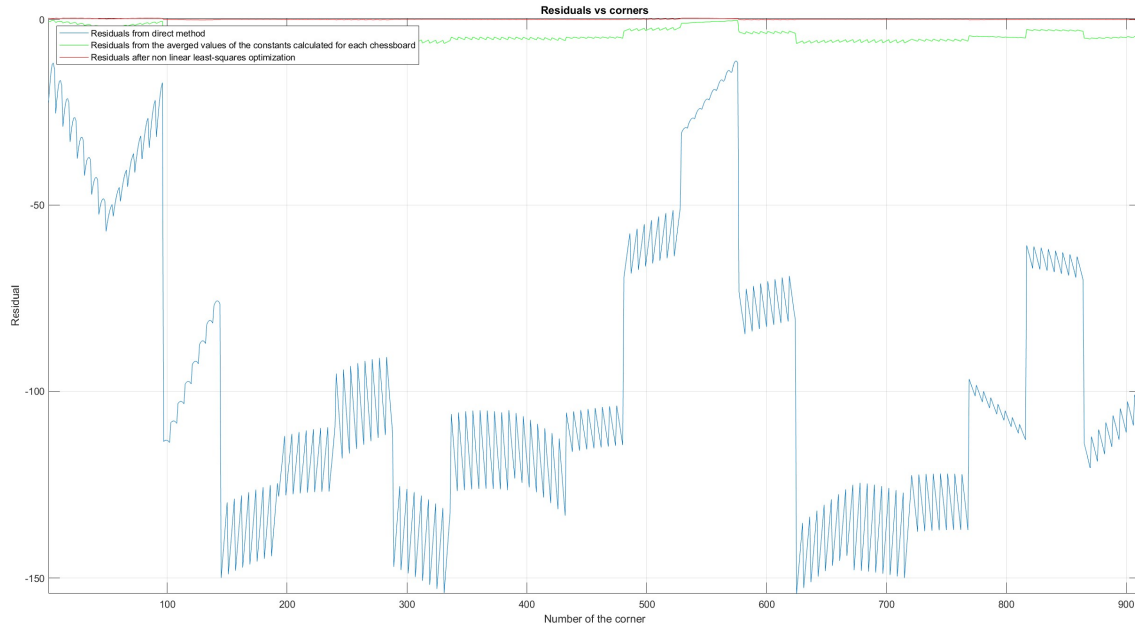


FIGURE 5.11 RESIDUALS FOR EACH CORNER OF THE SAMPLE. IN BLUE THE RESIDUALS OBTAINED WITH THE FIRST (DIRECT) METHOD, IN GREEN THE RESIDUAL USING THE AVERAGED VALUES OF THE CONSTANTS CALCULATED FOR EACH CHESSBOARD, IN RED THE RESIDUALS AFTER THE NONLINEAR LEAST-SQUARES EVALUATION

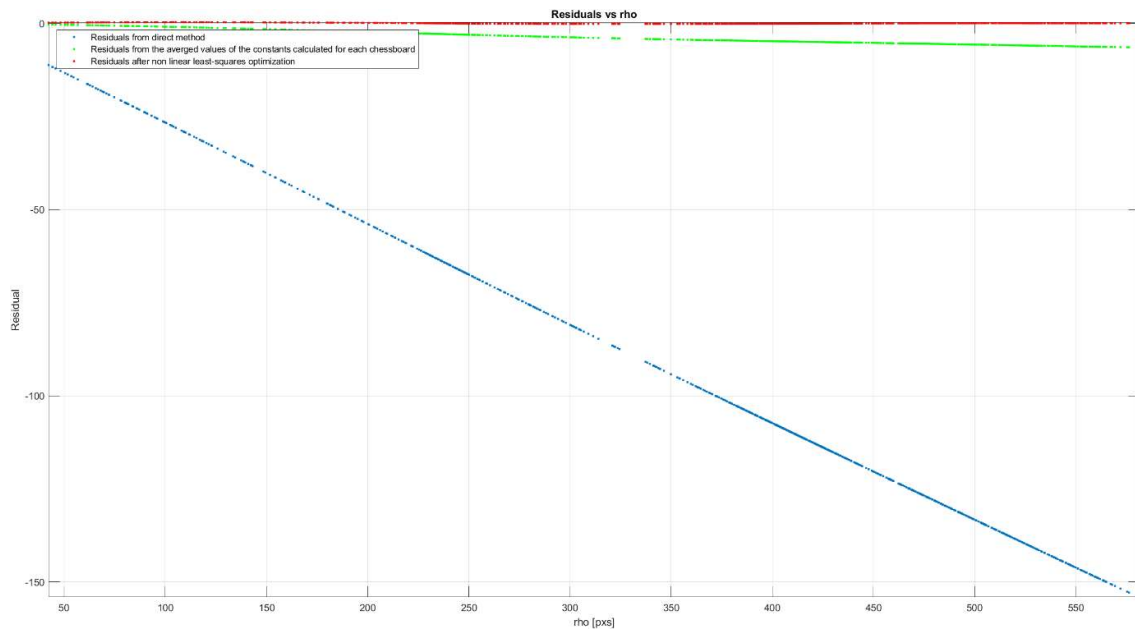


FIGURE 5.12 RESIDUALS DISTRIBUTION WITH RESPECT TO THE DISTANCE FROM THE CENTER OF THE LENS PROJECTION ON THE SENSOR. IN BLUE THE RESIDUALS OBTAINED WITH THE FIRST (DIRECT) METHOD, IN GREEN THE RESIDUAL USING THE AVERAGED VALUES OF THE CONSTANTS CALCULATED FOR EACH CHESSBOARD, IN RED THE RESIDUALS AFTER THE NONLINEAR LEAST-SQUARES EVALUATION

We can clearly see that the direct method was not able to obtain significantly good results, since the residuals are quite large with respect to the other methods. In Figure 5.13 and Figure 5.14 we show the same plots limited to the last methods.

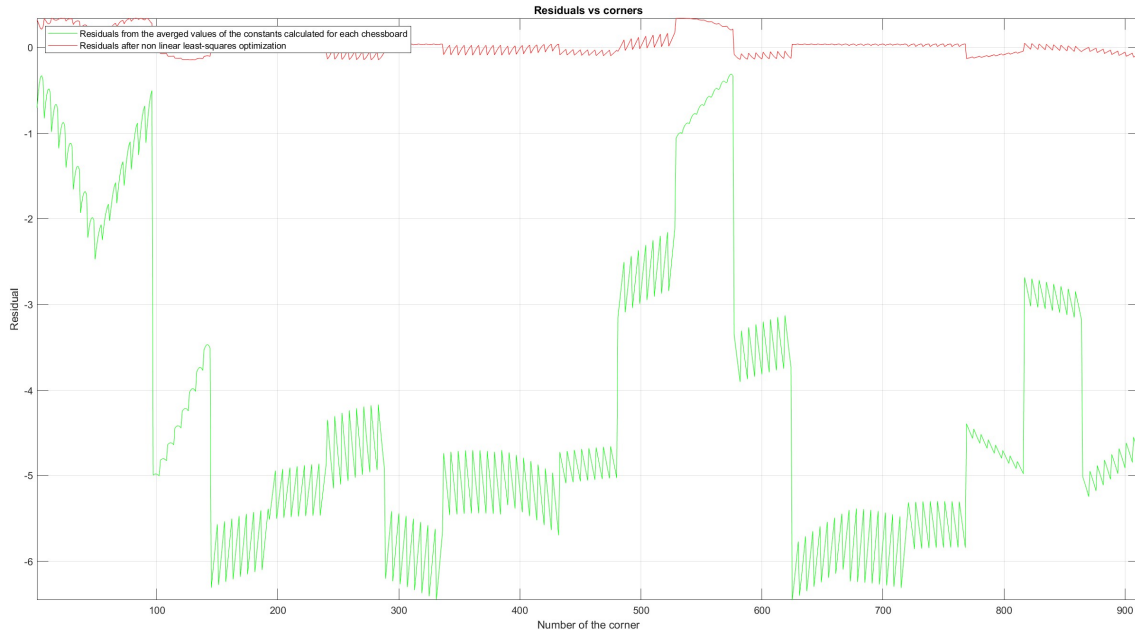


FIGURE 5.13 RESIDUALS FOR EACH CORNER OF THE SAMPLE. IN GREEN THE RESIDUALS USING THE AVERAGED VALUES OF THE CONSTANTS CALCULATED FOR EACH CHESSBOARD, IN RED THE RESIDUALS AFTER THE NONLINEAR LEAST-SQUARES EVALUATION

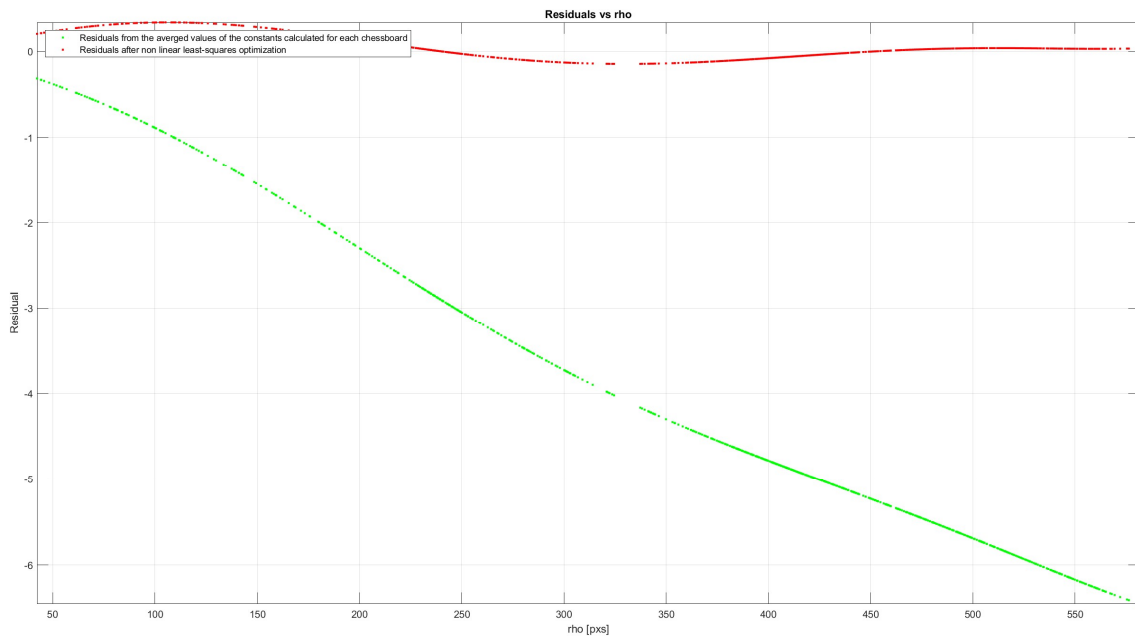


FIGURE 5.14 RESIDUALS DISTRIBUTION WITH RESPECT TO THE DISTANCE FROM THE CENTER OF THE LENS PROJECTION ON THE SENSOR. IN GREEN THE RESIDUAL USING THE AVERAGED VALUES OF THE CONSTANTS CALCULATED FOR EACH CHESSBOARD, IN RED THE RESIDUALS AFTER THE NONLINEAR LEAST-SQUARES EVALUATION

It is clear how much the nonlinear least-squares method improves the residuals, constraining the values of the constants.

It is possible to see that with this last method we are able to retrieve the same values for the constants even with random, although reasonable, starting values for k_2 and dk_1 . The following figures show the same plots of the

residuals with starting values $dk_1 = 5$ and $k_2 = 0.3$, resulting in the same dk_1 and k_2 found earlier after the nonlinear least-squares evaluation.

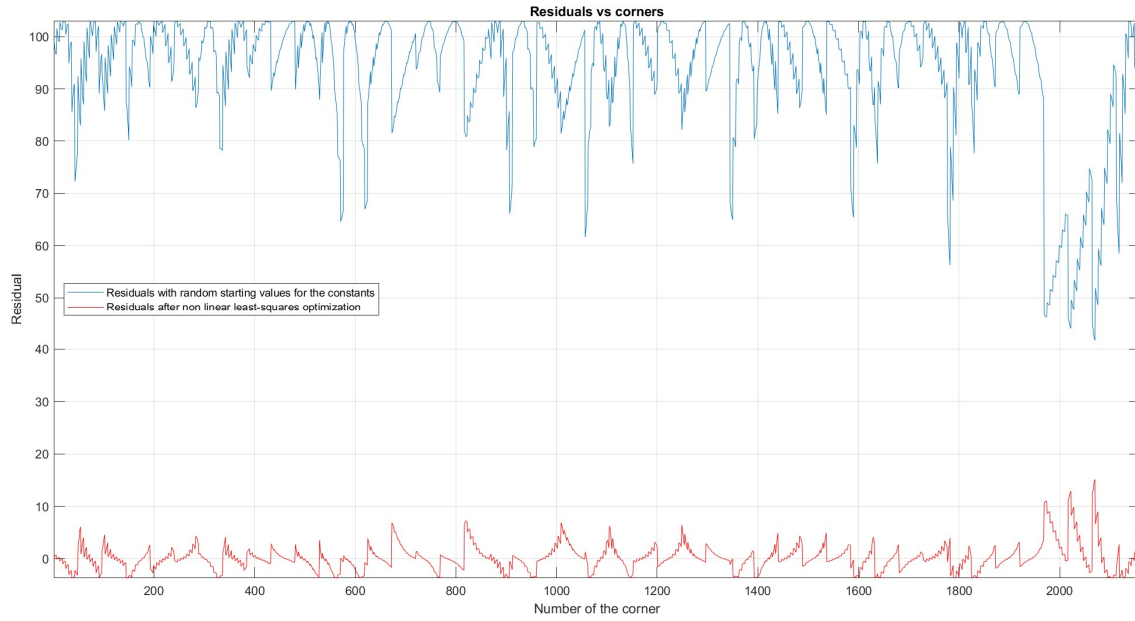


FIGURE 5.15 RESIDUALS FOR EACH CORNER OF THE SAMPLE, IN BLUE THE RESIDUALS FOR $dk_1 = 5$ AND $k_2 = 0.3$, IN RED THE RESIDUALS AFTER THE NONLINEAR LEAST-SQUARES EVALUATION

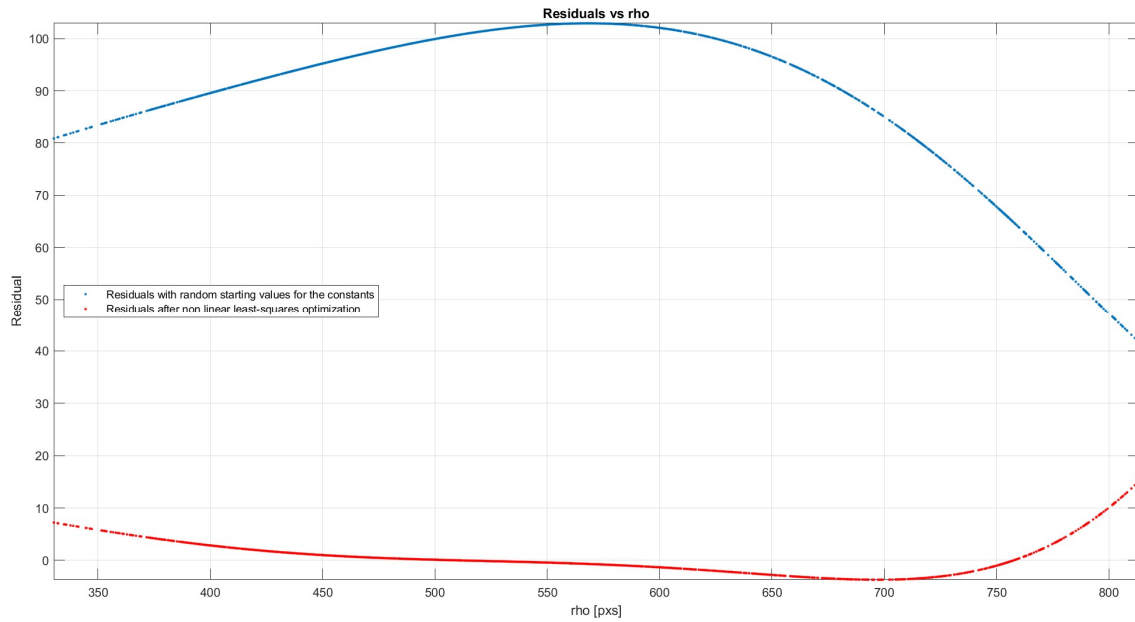


FIGURE 5.16 RESIDUALS DISTRIBUTION WITH RESPECT TO THE DISTANCE FROM THE CENTER OF THE LENS PROJECTION ON THE SENSOR, IN BLUE THE RESIDUALS FOR $dk_1 = 5$ AND $k_2 = 0.3$, IN RED THE RESIDUALS AFTER THE NONLINEAR LEAST-SQUARES EVALUATION

6 Table of data results

In this section are reported the most valuable parameters associated to each image as defined in this following reference table:

ID_IMAGE	#	name of the k-th image
MEAN_POS_i_REFC0	[px]	mean horizontal position in the lens reference system
MEAN_POS_j_REFC0	[px]	mean vertical position in the lens reference system
MEAN_POS_i	[px]	mean horizontal position in the sensor reference system
MEAN_POS_j	[px]	mean vertical position in the sensor reference system
AZ	[°]	mean azimuth angle
ZEN	[°]	mean zenith angle
DIST	[px]	mean corner distance from the center of the lens
ERR_i	[px]	mean vertical residual
ERR_j	[px]	mean horizontal residual
STD_i	[px]	standard deviation of the horizontal residuals
STD_j	[px]	standard deviation of the vertical residuals

ID IMAGE	MEAN POS_i (REFC0)	MEAN POS_j (REFC0)	MEAN POS_i	MEAN POS_j	AZ	ZEN	DIST	ERR_i	ERR_j	STD_i	STD_j
#	[px]	[px]	[px]	[px]	[°]	[°]	[px]	[px]	[px]	[px]	[px]
1	105.2978	-37.8083	1078.8163	1165.1525	-20.1721	15.9391	118.0819	0.0691	0.0663	0.4124	0.4018
2	-132.1824	-35.2568	841.3335	1167.7181	-104.4017	19.0216	140.8403	-0.0418	0.0527	0.2816	0.2299
3	-350.5054	-6.8154	623.0073	1196.1726	1.1188	47.8254	352.7852	0.0239	0.0774	0.2931	0.3395
4	-342.2471	-382.3193	631.2743	820.6681	-131.7948	69.9489	515.163	0.0278	0.0194	0.3416	0.2723
5	-112.8008	-429.4299	860.7242	773.5439	-104.7133	60.4364	445.496	-0.0159	-0.0543	0.2935	0.2101
6	116.5519	-365.5194	1090.078	837.4407	-72.3768	52.2633	385.434	0.0054	0.0176	0.2336	0.2178
7	-319.7961	412.7999	653.7075	1615.786	127.7241	71.2522	524.6832	0.0008	-0.0048	0.4906	0.4612
8	-19.9207	430.9078	953.5858	1633.876	92.6445	58.832	433.7118	0.0184	-0.0115	0.408	0.4109
9	229.7312	377.3115	1203.2417	1580.2649	58.7169	60.0994	443.0152	0.0522	0.0651	0.3175	0.3342
10	-53.5084	406.1923	919.9983	1609.1625	97.4968	55.6434	410.2959	0.0103	-0.0001	0.282	0.293
11	-72.0915	209.2047	901.4195	1412.176	108.9255	30.1046	222.4491	0.0198	0.0016	0.2829	0.18
12	-75.3282	10.6282	898.1873	1213.5997	51.7546	10.507	77.9636	0.0529	0.0094	0.249	0.1498
13	-79.1902	-272.1589	894.3316	930.8128	-106.1895	38.5187	284.319	-0.0007	-0.0025	0.2377	0.2954
14	-395.4376	-341.9025	578.0822	861.0882	-139.0981	71.2551	524.7069	0.0115	-0.0152	0.3608	0.2449
15	-363.4679	363.5069	610.0363	1566.4956	134.9838	70.1757	516.8153	0.0054	0.0148	0.3681	0.278
16	483.8468	-40.4585	1457.3696	1162.4797	-4.7787	66.0754	486.8374	0.0267	0.0768	0.4016	0.3603
17	271.2381	-280.9992	1244.764	921.9517	-45.9944	52.9799	390.7105	-0.0185	0.0107	0.2907	0.2441
18	233.9592	56.4301	1207.477	1259.3831	13.4994	32.6693	241.3065	0.0366	-0.0121	0.2236	0.2146
19	356.3603	207.5414	1329.8761	1410.4872	30.1498	55.996	412.8848	0.0166	0.0187	0.2475	0.243